SPE-209280-MS

Analyzing X-Ray CT Images from Unconventional Reservoirs Using Deep Generative Models

Yulman Perez Claro, Stanford University; Niccolo Dal Santo and Vignesh Krishnan, Mathworks, INC; Anthony Kovscek, Stanford University

Abstract

Characterization of rock samples is relevant to hydrocarbon production, geothermal energy, hydrogen storage, waste storage, and carbon sequestration. Image resolution plays a key role in both property estimation and image analysis. However, poor resolution may lead to underestimation of rock properties such as porosity and permeability. Therefore, improving the image resolution is paramount. This study shows the workflow for 2D image super-resolution processes using a Convolutional Neural Network (CNN) method. The rock samples used to test the networks were three unfractured Wolfcamp shales, a Bentheimer sandstone (Guan et al., 2019), and a Vaca Muerta (Frouté et al., 2020) shale. These samples were imaged with a clinical Computed Tomography (CT) scanner (100's µm resolution) as well a microCT scanner (10's µm resolution). This established training, validation, and test data sets. The deep learning architectures were implemented in Matlab 2021b. The network performance is calculated using two metrics: i) pixel signal to noise ratio (PSNR) and ii) structural similarity index method (SSIM). In addition, porosity values on the image data sets are presented to illustrate their relevance. Training options and different strategies for network tuning are also discussed in the results section. Results illustrate the potential for AI to improve the resolution of CT images by at least a factor of 4. This level of improvement is essential for resolving fractures, other permeable conduits in impermeable shale samples, and shale fabric features. We outline a pathway to greater improvement of resolution.

Introduction

Improving single image super-resolution has been a focus area for the Artificial Intelligence (AI) community (Kim et al., 2016; Da Wang et al., 2019; Yang et al., 2019). Super resolution has been considered by most researchers as a breakthrough in the area of digital rock analysis (Sun et al., 2019; Niu et al., 2020). The first approach for enhancing image resolution was the so-called traditional interpolation method (Rukundo and Cao, 2012). The key concept for interpolation was the generation of continuous values for a given function (Patel and Mistree, 2013) using different techniques. For example, nearest neighborhood (Ganin and Lempitsky, 2014), linear (Getreuer, 2011), or bicubic (Fadnavis, 2014) interpolation. These methods

were very useful because no additional information was required and the computational cost was relatively low.

A new generation of methods started with the success of Convolutional Neural Network (CNN) for tasks like image classification (Lee and Kwon, 2017), facial recognition (Yang et al., 2018), and object detection (Ren et al., 2016). Dong et al. (2015) proposed a method that was mainly focused on representing a deep CNN with a low-resolution image as input and a high-resolution image as output. In addition, they proposed a methodology to test hyperparameters for the network to increase speed and trade-off the performance. This particular CNN was called SRCNN –a super-resolution convolutional neural network.

The SRCNN method is fast and accurate for super-resolution tasks. However, it was not able to capture the finest features in the image. Goodfellow et. al., (2016) introduced the Generative Adversarial Network (GAN) framework. It was an approach with two simultaneous models where a generative model, G, captures the data distribution and a discriminative model D that acts as a discriminator. The high-resolution output image showed the best performance among the state-of-the-art methods for 4X up-scaling factor. The authors used a perceptual loss function for both the adversarial and content loss. In addition, the previous method used a discriminator to determine if the generated image was real or fake. Even though some applications of super-resolution have been extensively explored, implementation in the area of earth sciences and specifically to rock image analysis leading to digital rock physics applications is still immature.

This study proposes and illustrates a workflow beginning from data acquisition for 2D image super-resolution using a CNN. The network's performance is calculated using two metrics: i) pixel to noise signal ratio (PSNR) and ii) structural similarity index method (SSIM). Shale and sandstone rock samples are used to evaluate performance. Shale images are at the resolution of the shale fabric. That is, pores and microfractures are below the resolution of the instrument. On the other hand, sandstone images display pores and grains.

Data Acquisition and Preparation

The shale samples used to test the networks are shown in Fig. 1 and the rock properties are listed in Table 1. The bulk density and grain density were calculated from mercury injection capillary pressure (MICP) experiments. These samples are unconventional rocks from the Hydraulic Fracturing Test Site (HFTS) in the Midland Basin, TX (Ciezobka et al., 2018; Zhang et al., 2021; NETL, 2021).

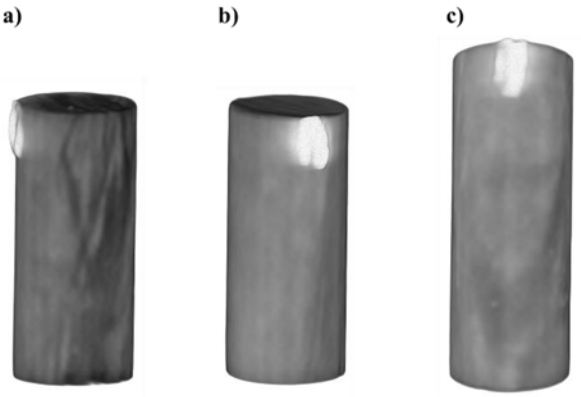

Figure 1—Wolfcamp unconventional formation samples. Micro-CT image three-dimensional reconstructions: a) HK-4-2a, b) HK-4-2c, and c) HK-4-3b.

Table 1—Wolfcamp unconventional formation sample properties.

	HK-4-2a	HK-4-2c	HK-4-3b
Sample Depth, ft	9602.2	9602.2	9652.1
Diameter, cm	2.54	2.54	2.54
Length, cm	5.6	5.6	6.9
Bulk density, g/mL	2.33	2.34	2.37
Grain density, g/mL	2.61	2.61	2.64
*Matrix Porosity, %	10.7	10.3	10.2

The samples were imaged with a clinical Computed Tomography (CT) GE High-Speed IV Generation CT scanner at 140 kV with 195 × 195 × 625 μm voxel resolution as well a micro-CT Zeiss Xradia 520 Versa scanner at 140 kV with 27 × 27 × 27 μm voxel resolution. The images were cleaned and aligned using the processing tools from Matlab 2021®, including a circular mask to remove the background pixels and a particle swarm optimization method for image rotation and alignment in the z-direction. Figure 2 shows 4 image pairs completely aligned and normalized. The histograms are also included where the zero values were excluded from the normalization.

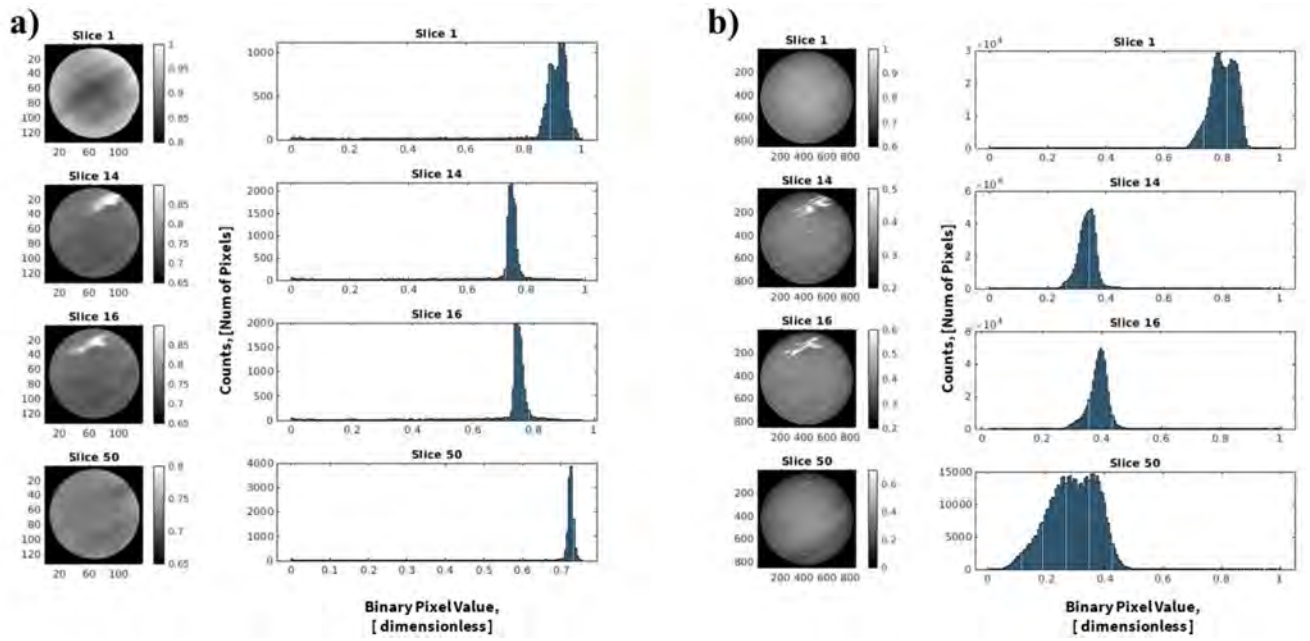

Figure 2—Image pairs for the sample HK-4-3b: a) lower resolution CT and b) greater resolution micro-CT.

Methods

The workflow was implemented in Matlab 2021b using the docker option from Amazon cloud S3 services. An NVIDIA Deep Learning AMI instance (p3.2xlarge) was executed with a 32GB capacity in AWS, Amazon. The network architecture was adapted from Da Wang et al. (2019) with modifications of the filter size, the activation functions, and the training parameters. The CNN network was built using the Deep Network Designer tool from Matlab 2021b and the training data set was connected using the Matlab Drive tool. Initially, the structure was generated using the developer tool and its dimensionality was confirmed with the Analyze Network option to confirm consistency between the inputs. The network inputs 2D images with pixel sizes of [50 × 50] and outputs a [200 × 200] high-resolution image. The CNN network was implemented in Matlab 2021b cloud services because the training process requires a Graphic Processing

Unit (GPU). The images were stored in buckets within AWS services and then input into the main code using the image Datastore function from Matlab. A key modification to the CNN is the activation function and batch normalization after each convolutional layer except the first. The network has a total of 61 layers and 68 connections. The network architecture implemented is presented in Fig. 3.

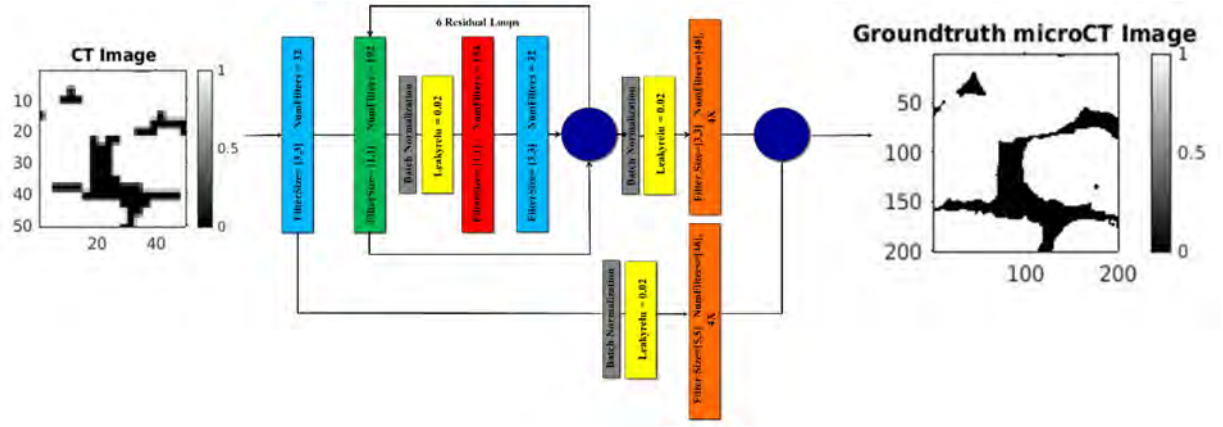

Figure 3—CNN architecture for image super-resolution. Architecture modified from Da Wang et al. (2019). CT images are representative of granular media such as sandstone and not unconventional formations.

Figure 3 shows the specific details about the filter size and the number of filters for each convolution layer. The network was trained on patches of [200 × 200] pixel size, using an augmenter for reflection and rotation to increase significantly the number of images in the training data set. All the images were stored in Amazon cloud services, and then a docker in AWS cloud services was used to train the model and save the results. Table 2 shows the details for all the parameters for the training options. The training time for the network was around 19 hrs.

Table 2—CNN Network Training Options

Training Options	
Max Epochs	50
Epoch Intervals	1
Initial Learning Rate	0.0001
Learning Rate Factor	0.1
L2 reg	0.0001
Minibatch Size	16
Optimizer	Adam
Validation Data	Imds Validation

In addition to the Wolfcamp formation images, Bentheimer sandstone images (Guan et al., 2019) and a Vaca Muerta unconventional rock data set (Frouté et al., 2020) were tested using the Rock Flow model (Anderson et al., 2020). The Rock Flow model is a deep learning method based on generative flow models where 2D data is used for creating a grayscale volume. Details about its structure and implementation to generate synthetic data can be found elsewhere (Anderson et al., 2020). The two samples were evaluated following Anderson et al.'s (2020) future work advice to train/test the Rock Flow model using different samples data sets. The Bentheimer sandstone sample is used as a reference due to the large number of features. Similarly, the Vaca Muerta sample provides valuable information about the interconnected pore network (~ nanometer scale). Two different batches sizes were evaluated for the network training, 16 × 16

and 8 × 8. The 16 × 16 batch size has a training time of around ~16 hours whereas the 8 × 8 batch size can be a least more than ~30 hrs. A small batch size generates images with the finest details; however, it implies a longer training time.

Results and Discussion

Figure 4 shows the network output for the relatively homogeneous HK-4-3b shale sample. The network results were in all cases compared with an image obtained from bicubic interpolation. The interpolated image gives a baseline to evaluate the network performance or adjust the training options. The metrics of the pixel to noise signal ratio (PSNR) and the structural similarity index method (SSIM) were also computed for all the images from bicubic interpolation. Figure 4 shows two images for the unfractured HK-4-3b shale sample. The network output shows an increment in both metrics, PSNR and SSIM. However, the finest features are not captured by the network. The image in the second row is a case where there are not many heterogeneous features. Consequently, the super-resolution model struggles because there are not many details for the network to learn. Therefore, there is limited image enhancement, and the model does not capture the finest details. The PSNR increases up to 17 and the SSIM up to 0.688. The shale sample images show a qualitative improvement in the image texture for the high-density region. To validate the hypothesis about the poorer model performance due to the features of the samples, two data sets were considered: both grayscale and binarized sandstone samples. Results for a binarized sandstone sample are given in Fig. 5 and those for a grayscale representation of sandstone in Fig. 6.

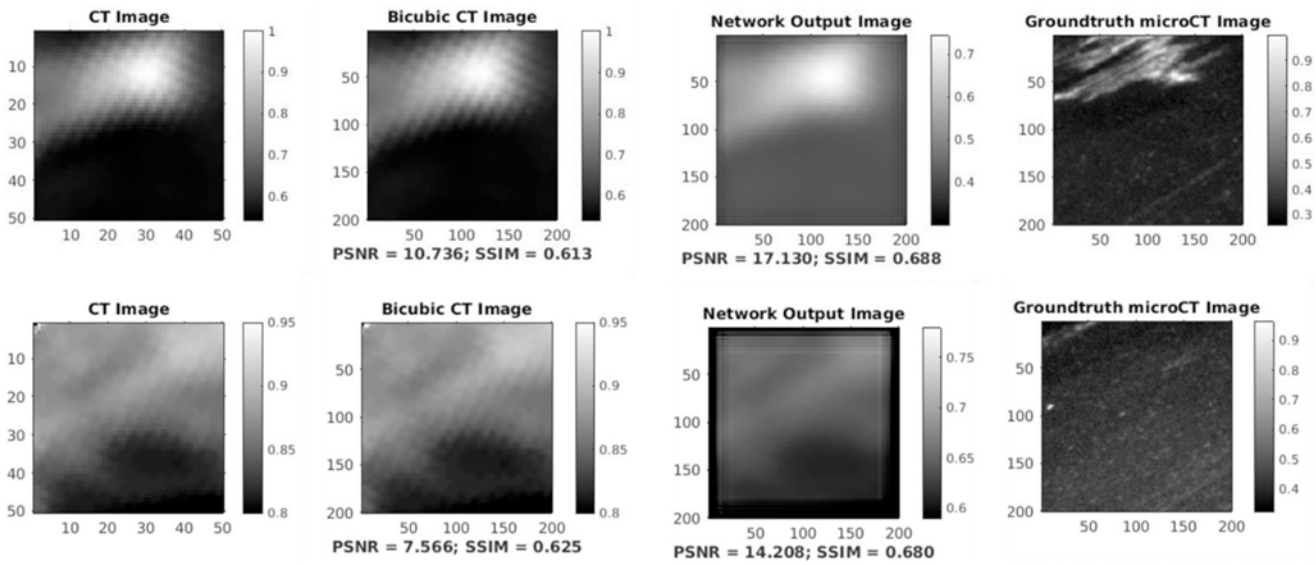

Figure 4—HK-4-3b Shale sample output test.

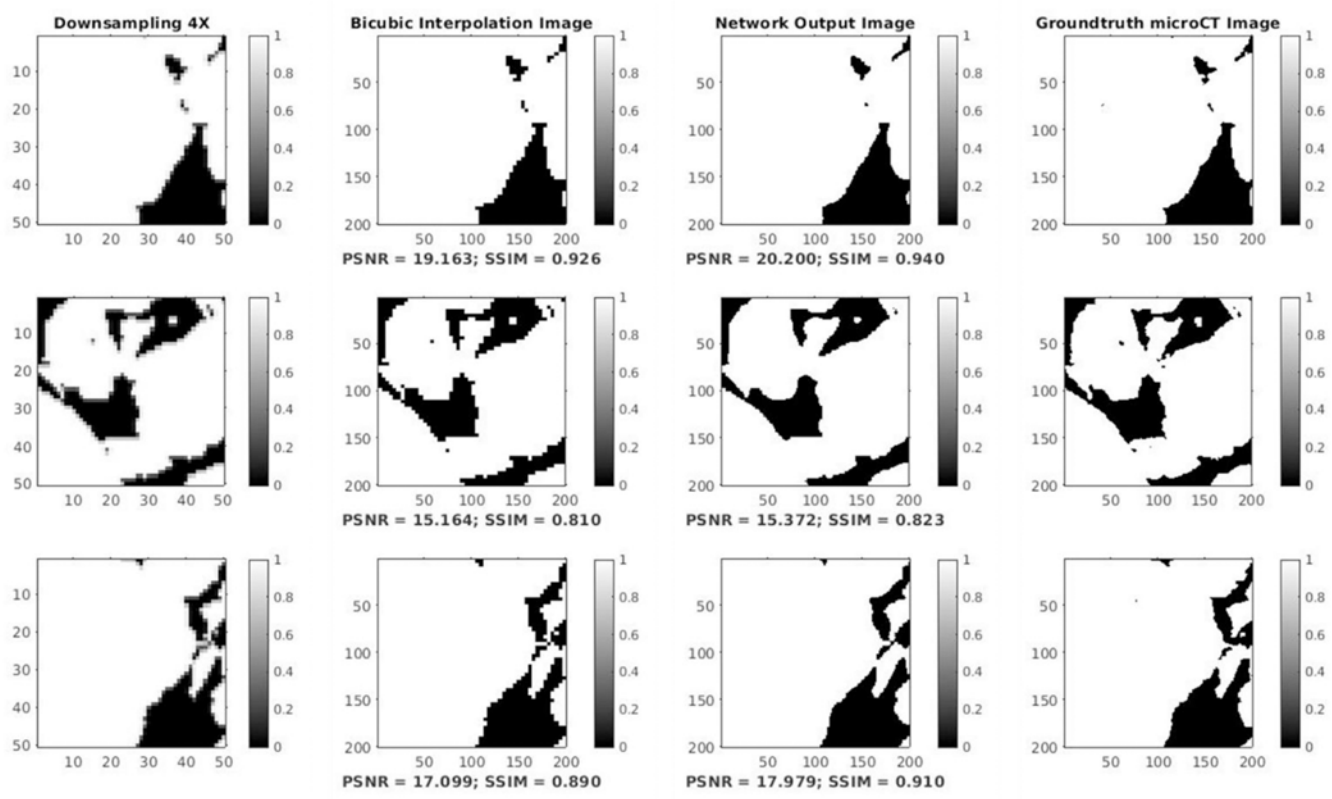

Figure 5—Network performance using a binarized Bentheimer sandstone sample.

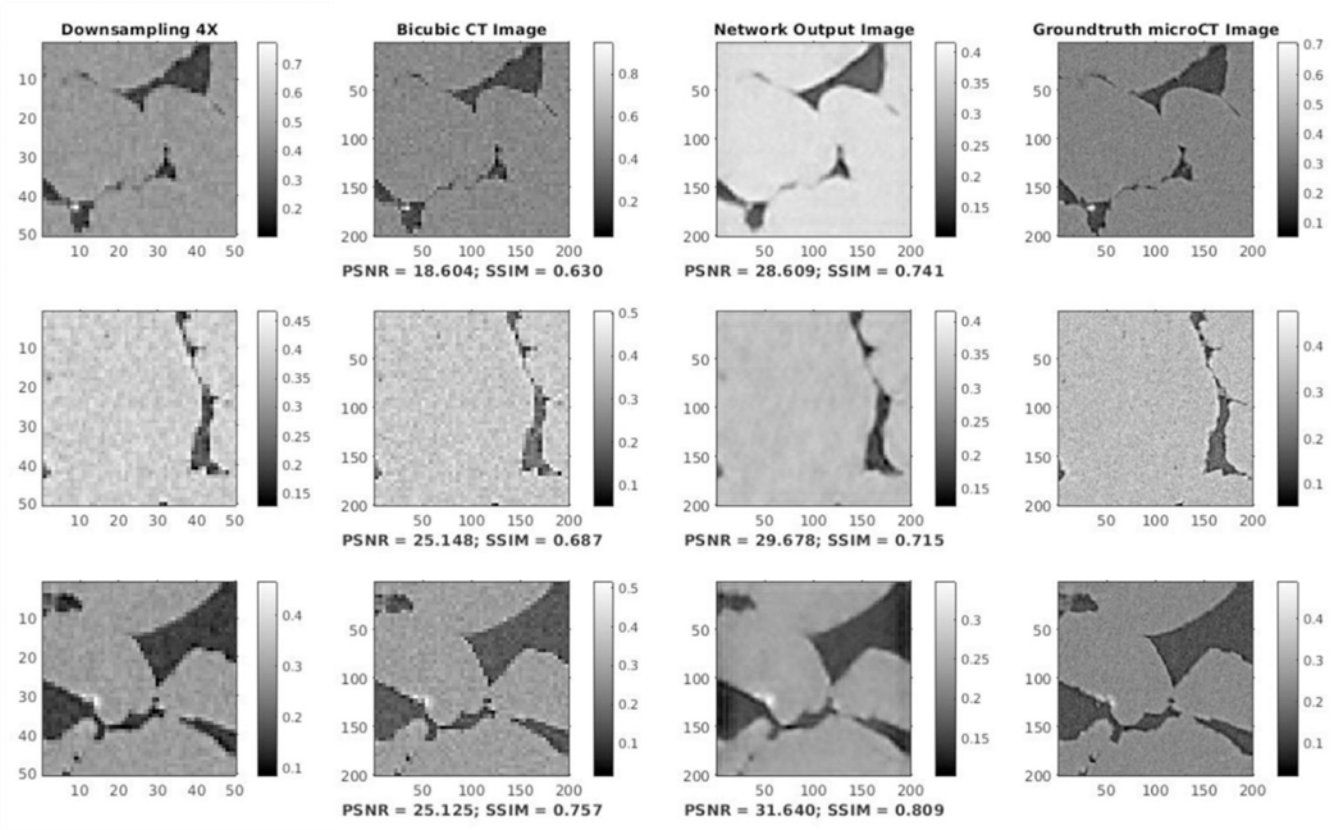

Figure 6—Network performance from a grayscale Bentheimer sandstone sample.

The next image data set, Fig. 5, are representative results from binarized images of a Bentheimer sandstone. Grains are white and the pore space is black. The improvement for the network output versus the bicubic interpolation is more significant with the grayscale images than with the binarized images. Clearer details on the edges of grains emerged and the predictions are closer to the ground truth. A key point to discuss is the fact that the network outputs an image in grayscale rather than a binarized image. However, the grayscale results are not a limitation because a threshold could be defined and binarized images obtained from the network output. The results shown here already included the threshold.

Images in Fig. 6 show a clear improvement in resolution. Compare the CT images on the left with the network output images, the features are properly captured in comparison to the microCT images. The network for these two cases was trained with a downsampling set of 4X to simulate the CT images, work in progress will include very heterogeneous samples captured with both scanning techniques, X-ray CT and microCT. It is very important to mention that details such as microcracks or pores below the ground truth resolution cannot be capture. The values for the PSNR ranged between 18.604 to 25.148 for the bicubic interpolation, and in a range between 28.609 to 31.640 for the output images. In the same case as the other metric, the values for SSIM ranged between 0.630 to 0.757 for the bicubic interpolation, and in a range between 0.715 to 0.809 for the output images.

The previous metrics validate the network implementation for representation of shapes; however, a clear petrophysical measure should be considered to evaluate the performance as related to rock properties. In that sense, porosity estimation for the images was implemented using a threshold as is shown in Fig. 7. With the threshold defined, the images were binarized. Then, the total number of pixels under the threshold was known and the porosity was calculated as the ratio of the number of pixels under the threshold to the total number of pixels.

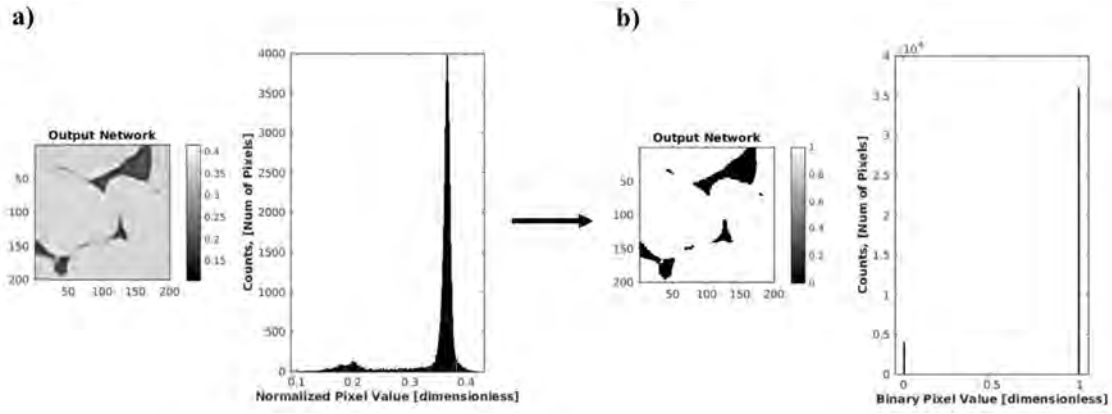

Figure 7—Threshold for the porosity estimation after using the network: a) grayscale output image and b) binarized output image.

The previous procedure was applied to the other three images: network input (downsampling 4x), image from bicubic interpolation, and ground truth. The results for the porosity are shown below the image in Fig. 8. The impact of sharpening the image quality (high resolution) and thus estimating petrophysical properties as porosity is shown. There is still room for improvement since the porosity for the network output at 7.13% is not the same as the ground truth of 7.61%; however, a framework has been outlined for further development.

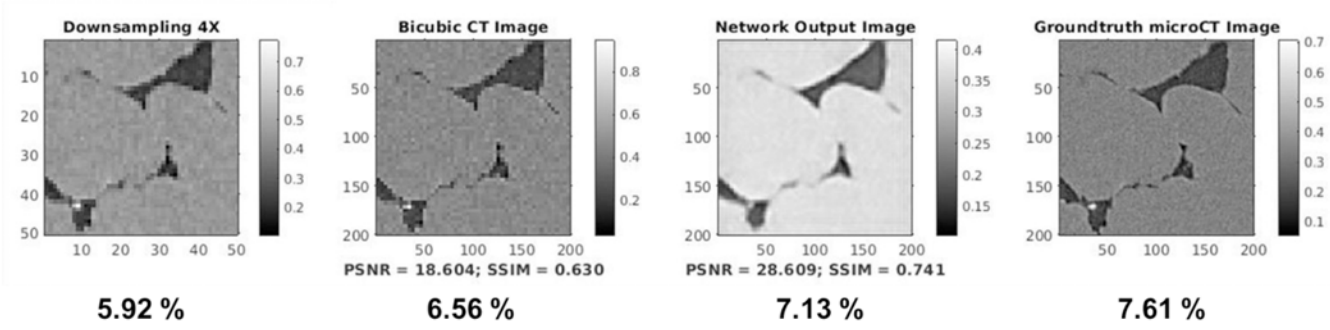

Figure 8—Porosity effect on an image data set.

Conclusions and Future Work

This study concludes that AI methods are able to improve the image resolution of CT images of different rock types. The pixel to noise signal ratio (PSNR) and the structural similarity index methods (SSIM) confirm an improvement in the resolution. Results illustrate the potential for AI to improve the image resolution of CT images by at least a factor of 4. This level of improvement is essential for resolving fractures, other permeable conduits in impermeable shale samples, and shale fabric features. We outline a pathway to greater improvement of resolution.

Future work includes establishing algorithms for super-resolution of images of fully saturated rocks. The previous cases have shown an improvement in resolution for dry, vacuumed samples. Now, the task is to calculate high-resolution images including rock-fluid interactions. Super resolution will be very valuable to understand liquid diffusion processes within the rock matrix. The baseline to achieve the previous objective is to collect a set of data from different samples (sandstone, carbonate, chalk, limestone) with many features. The data has been recently collected and the image processing is still ongoing work, Fig. 9.

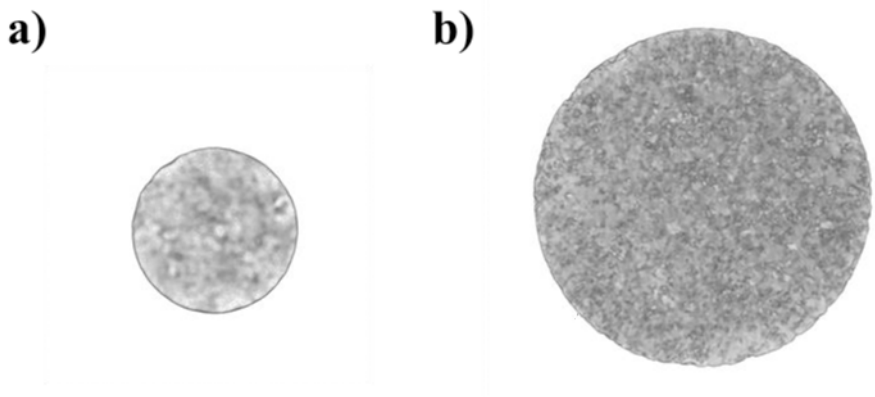

Figure 9—Data acquisition for a limestone sample: a) CT and b) micro-CT image.

Acknowledgments

This work was supported by the Center for Mechanistic Control of Water-Hydrocarbon-Rock Interactions in Unconventional and Tight Oil Formations (CMC-UF), an Energy Frontier Research Center from the U.S. Department of Energy (DOE), Office of Science under Award # DE-SC0019165. Additional support came from MathWorks along with many insightful technical discussions. Part of this work was performed at the Stanford Nano Shared Facilities (SNSF), supported by the National Science Foundation under award ECCS-1542152.

References

Anderson, T. I., Guan, K. M., Vega, B., Aryana, S. A., & Kovscek, A. R. (2020). RockFlow: Fast generation of Synthetic Source Rock Images Using Generative Flow Models. *Energies*, **13**(24), 6571.

Chao Dong, Chen Change Loy, Kaiming He, and Xiaoou Tang. 2015. Image super-resolution using deep convolutional networks. *IEEE transactions on pattern analysis and machine intelligence*, **38**(2):295–307.

Christian Ledig, Lucas Theis, Ferenc Husz źar, Jose Caballero, Andrew Cunningham, Alejandro Acosta, Andrew Aitken, Alykhan Tejani, Johannes Totz, Zehan Wang, et al. 2017. Photo-realistic single image super-resolution using a generative adversarial network. In Proceedings of the IEEE conference on computer vision and pattern recognition, pages 4681–4690.

Ciezobka, J., Courtier, J., & Wicker, J. (2018, July). Hydraulic fracturing test site (HFTS)-project overview and summary of results. In SPE/AAPG/SEG Unconventional Resources Technology Conference. OnePetro.

Da Wang, Y., Armstrong, R., & Mostaghimi, P. (2019). Super-resolution convolutional neural network models for enhancing the resolution of rock micro-ct images. arXiv preprint arXiv:1904.07470.

Frouté L, Wang Y, McKinzie J, Aryana SA, Kovscek AR. Transport Simulations on Scanning Transmission Electron Microscope Images of Nanoporous Shale. *Energies*. 2020; **13**(24):6665. https://doi.org/10.3390/en13246665

Goodfellow, I., Bengio, Y., & Courville, A. (2016). *Deep learning*. MIT press.

Guan, K.M., Nazarova, M., Guo, B. et al. Effects of Image Resolution on Sandstone Porosity and Permeability as Obtained from X-Ray Microscopy. *Transp Porous Med* **127**, 233–245 (2019). https://doi.org/10.1007/s11242-018-1189-9

Huafeng Sun, Hadi Belhaj, Guo Tao, Sandra Vega, and Luofu Liu. 2019. Rock properties evaluation for carbonate reservoir characterization with multi-scale digital rock images. *Journal of Petroleum Science and Engineering*, **175**:654–664.

Hydraulic Fracturing Test Site (HFTS). NETL, *netl.doe.gov*. (2021). Retrieved January 24, 2022, from https://netl.doe.gov/node/1989

Hyungtae Lee and Heesung Kwon. 2017. Going deeper with contextual cnn for hyperspectral image classification. *IEEE Transactions on Image Processing*, **26**(10):4843–4855.

Jiwon Kim, Jung Kwon Lee, and Kyoung Mu Lee. 2016. Accurate image super-resolution using very deep convolutional networks. In Proceedings of the IEEE conference on computer vision and pattern recognition, pages 1646–1654.

Kim, J., Lee, J. K., & Lee, K. M. (2016). Accurate image super-resolution using very deep convolutional networks. In Proceedings of the IEEE conference on computer vision and pattern recognition (pp. 1646–1654).

Niu, Y., Mostaghimi, P., Shabaninejad, M., Swietojanski, P., & Armstrong, R. T. (2020). Digital rock segmentation for petrophysical analysis with reduced user bias using convolutional neural networks. *Water Resources Research*, **56**(2), e2019WR026597.

Olivier Rukundo and Hanqiang Cao. 2012. *Nearest neighbor value interpolation*. arXiv preprint arXiv:1211.1768.

Pascal Getreuer. 2011. Linear methods for image interpolation. *Image Processing On Line*, **1**:238–259.

Saxena, N., Hows, A., Hofmann, R., Alpak, F. O., Freeman, J., Hunter, S., & Appel, M. (2018). Imaging and computational considerations for image computed permeability: operating envelope of digital rock physics. *Advances in Water Resources*, **116**, 127–144.

Shaoqing Ren, Kaiming He, Ross Girshick, and Jian Sun. 2016. Faster r-cnn: towards real-time object detection with region proposal networks. *IEEE transactions on pattern analysis and machine intelligence*, **39**(6):1137–1149.

Shreyas Fadnavis. 2014. Image interpolation techniques in digital image processing: an overview. *International Journal of Engineering Research and Applications*, **4**(10):70–73.

Vaishali Patel and Kinjal Mistree. 2013. A review on different image interpolation techniques for image enhancement. *International Journal of Emerging Technology and Advanced Engineering*, **3**(12):129–133.

Wenming Yang, Xuechen Zhang, Yapeng Tian, Wei Wang, Jing-Hao Xue, and Qingmin Liao. 2019. Deep learning for single image super-resolution: A brief review. *IEEE Transactions on Multimedia*, **21**(12):3106–3121.

Yang, W., Zhang, X., Tian, Y., Wang, W., Xue, J. H., & Liao, Q. (2019). Deep learning for single image super-resolution: A brief review. *IEEE Transactions on Multimedia*, **21**(12), 3106–3121.

Yaroslav Ganin and Victor Lempitsky. 2014. Fields: Neural network nearest neighbor fields for image transforms. In Asian Conference on Computer Vision, pages 536–551. Springer.

Yufu Niu, Peyman Mostaghimi, Mehdi Shabaninejad, Pawel Swietojanski, and Ryan T Armstrong. 2020. Digital rock segmentation for petrophysical analysis with reduced user bias using convolutional neural networks. *Water Resources Research*, **56**(2):e2019WR026597.

Yu-Xin Yang, Chang Wen, Kai Xie, Fang-Qing Wen, Guan-Qun Sheng, and Xin-Gong Tang. 2018. Face recognition using the sr-cnn model. *Sensors*, **18**(12):4237.

Zhang, Z., DiSiena, J., Bevc, D., Ning, I. L. C., Tan, Y., Swafford, L., … & Vissotski, A. (2021, July). Hydraulic fracture characterization by integrating multidisciplinary data from the Hydraulic Fracturing Test Site 2 (HFTS-2). In SPE/AAPG/SEG Unconventional Resources Technology Conference. OnePetro.